the center-to-limb variation also fits at each phase angle, we can have some confidence in the vertical structure as well. We are obviously still some way from having reduced all our data in both colors and compared it to these types of models; we have approximately 20,000 polarization measurements. Nevertheless, we believe the values derived here for the location of the $\tau = 1$ level of the aerosols and their scale height at equatorial latitudes are reasonably close to the final value we will obtain. The present example demonstrates the usefulness of these data.

T. GEHRELS, L. R. BAKER
E. BESHORE, C. BLENMAN
J. J. BURKE, N. D. CASTILLO
B. DACOSTA, J. DEGEWIJ
L. R. DOOSE, J. W. FOUNTAIN
J. GOTOBED, C. E. KENKNIGHT
R. KINGSTON, G. MCLAUGHLIN
R. MCMILLAN, R. MURPHY
P. H. SMITH, C. P. STOLL
R. N. STRICKLAND, M. G. TOMASKO
M. P. WIJESINGHE
University of Arizona, Tucson 85721
D. L. COFFEEN
Goddard Institute for Space Studies, New York 10025
L. ESPOSITO
Laboratory for Atmosphere and Space Physics, University of Colorado, Boulder 80309

References and Notes

1. T. Gehrels *et al.*, *Science* **183**, 318 (1974).
2. A. L. Baker *et al.*, *ibid.* **188**, 468 (1975).
3. S. F. Pellicori, E. E. Russell, L. A. Watts, *Appl. Opt.* **12**, 1246 (1973). A further discussion of spin-scan imaging is given by E. E. Russell and M. G. Tomasko [in *Chemical Evolution of the Giant Planets*, C. Ponnamperuma, Ed. (Academic Press, New York, 1976)].
4. Review chapters by M. G. Tomasko and T. Gehrels, in *Jupiter*, T. Gehrels, Ed. (Univ. of Arizona Press, Tucson, 1976).
5. P. H. Smith and L. R. Doose, *Sky Telesc.* **58**, 405 (1979).
6. J. J. Burke and R. N. Strickland, in preparation.
7. H. J. Reitsema, *Nature (London)* **272**, 601 (1978).
8. P. Guérin, *Icarus* **19**, 202 (1973).
9. I. R. Ferrín, *ibid.* **22**, 159 (1974).
10. Adjacency effects are due to the lateral diffusion of fresh developer toward a region of higher exposure. The density on the edge of the high-exposure region is therefore increased. The counterflow of developer by-products retards the development in the region next to the high-density edge. See R. S. Barrows and R. W. Wolfe, *Photogr. Sci. Eng.* **15**, 472 (1971).
11. A. F. O'D. Alexander, *The Planet Saturn* (Faber & Faber, London, 1962), p. 178.
12. B. A. Smith *et al.*, *Icarus* **25**, 466 (1975).
13. W. Fillius, W. H. Ip, C. E. McIlwain, *Science* **207**, 425 (1980); J. A. Simpson, T. S. Bastian, D. L. Chenette, G. A. Lentz, R. B. McKibbin, K. R. Pyle, A. J. Tuzzolino, *ibid.*, p. 411; J. A. Van Allen, M. F. Thomsen, B. A. Randall, R. L. Rairden, C. L. Grosskreutz, *ibid.*, p. 415.
14. Y. Kawata and W. M. Irvine, *Icarus* **24**, 472 (1975); L. W. Esposito and K. Lumme, *ibid.* **31**, 157 (1977); ——, W. D. Benton, L. J. Martin, H. M. Ferguson, D. T. Thompson, S. E. Jones, *Astron. J.* **84**, 1468 (1979).
15. J. D. Anderson, G. W. Null, E. D. Biller, S. K. Wong, W. B. Hubbard, J. J. MacFarlane, *Science* **207**, 449 (1980).
16. J. N. Cuzzi, R. H. Durisen, J. A. Burns, P. Hamill, *Icarus* **38**, 54 (1979).
17. J. N. Cuzzi and J. R. Pollack, *ibid.* **33**, 233 (1978).
18. J. W. Fountain and S. M. Larson, *ibid.* **36**, 92 (1978).
19. The position of Janus is unknown for 1979 (that is, the error in orbital phase is > 180°). The satellite discovered by Fountain and Larson (*18*) should be denoted as 1966 S 2, rather than as Saturn 11, as it is sometimes called; its position is also uncertain. The present radius of 2.53 R_S is close to that derived by Fountain and Larson for 1966 S 2.
20. *The International Astronomical Union Circular 3417* of 25 October 1979 has the announcements of 1979 S 1, the F ring, and the Pioneer division.
21. W. H. Blume *et al.*, in preparation. At the Pioneer Project Office, we received considerable help with the problems of the satellite's orbit from J. W. Dyer.
22. D. L. Harris, in *Planets and Satellites*, G. P. Kuiper and B. M. Middlehurst, Eds. (Univ. of Chicago Press, Chicago, 1961), p. 310; D. P. Cruikshank, in *The Saturn System*, D. M. Hunten and D. Morrison, Eds. (Conf. Publ. 2068, National Aeronautics and Space Administration, Washington, D.C., 1977), p. 238.
23. J. Bergstralh and G. Orton, *Bull. Am. Astron. Soc.* **11**, 554 (1979).
24. W. Macy, *Icarus* **32**, 328 (1977).
25. M. G. Tomasko, R. A. West, N. D. Castillo, *ibid.* **33**, 558 (1978).
26. We are indebted for their support to R. P. Hogan and others at the Pioneer Project Office, the Bendix Corporation, and NASA's Deep Space Network, which allowed us to receive the best possible data. We thank Pioneer Project manager C. F. Hall and Pioneer contracting officer J. F. Pogue for supporting the modeling of the Jupiter atmosphere in order to learn for the Saturn encounter. We are also indebted to the Santa Barbara Research Center for the competent design and construction of the instrument, which performed so well over such a long time. Finally, we thank W. B. Hubbard and B. A. Smith for refereeing this report.

3 December 1979

Pioneer Saturn Infrared Radiometer: Preliminary Results

Abstract. *The effective temperature of Saturn, 94.4 + 3 K, implies a total emission greater than two times the absorbed sunlight. The infrared data alone give an atmospheric abundance of H_2 relative to H_2 + He of 0.85 ± 0.15. Comparison of infrared and radio occultation data will give a more precise estimate. Temperature at the 1-bar level is 137 to 140 K, and 2.5 K differences exist between belts and zones up to the 0.06-bar level. Ring temperatures range from 60 to 70 K on the south (illuminated) side and from < 60 to 67 K in the planet's shadow. The average temperature of the north (unilluminated) side is ~ 55 K. Titan's 45-micrometer brightness temperature is 80 ± 10 K.*

Objectives of the infrared radiometer (IRR) experiment are (i) to measure the temperatures and heat balance of Saturn, its rings, and Titan; (ii) to search for horizontal temperature contrast on Saturn; (iii) to infer the atmospheric H_2 to He ratio; and (iv) possibly to infer characteristics of particles in the rings, such as size, thermal inertia, and out-of-plane motion. The instrument, consisting of two broadband channels centered at 20- and 45-μm wavelength, was described in reports following the Jupiter encounters (*1, 2*). The two beams scan at a fixed 75° angle with respect to the forward (that is, away from Earth) spin axis of the spacecraft. A scan consists of 33 observations (words) from a preselected 59° sector of the spacecraft spin cycle. The motion of the spacecraft causes a displacement of scans on the object to be viewed. A simultaneous 20- and 45-μm pair of images were made of Saturn and its rings during the 2.5-hour interval before closest approach (Fig. 1). These ~ 2×10^4 observations (10^4 in each channel), plus about 30 observations during which Titan partly filled the field of view, constitute the IRR data set from the Saturn encounter.

Table 1. Equivalent blackbody temperatures.

Temperature category	Belt (9°S to 12°S)	Zone (0° to 3°S)
T_{20}	91.4 K	89.2 K
T_{45}	99.5 K	97.0 K
$1/2(T_{20} + T_{45})$	95.5 K	93.1 K
T_e (model)	95.6 K	93.2 K
Average T_e	94.4 ± 3 K	

The instrument appears to have functioned correctly during the encounter. The signal when viewing space and the signal when viewing the internal calibration shutter at the known instrument temperature were both normal. The inferred instrument response differed from the laboratory value by less than 3 percent. The noise of a single observation is ± 2 data numbers (DN), equivalent to ± 3.0 K at 20 μm and ± 1.3 K at 45 μm for an object at 100 K, and to ± 3.0 K at 45 μm for an object at 70 K. A brightness temperature of 55 K corresponds to DN(45) = 2.9, which is exceeded 5 percent of the time when viewing space.

The results reported here are preliminary in that we have not computed the instrument pointing from the most recent trajectory analysis, which became available during preparation of this manuscript. For views of the rings at very small instrument elevation angles (for example, near ring plane crossing), and for views of the planet close to the limb, trajectory uncertainties are important.

The data on the Saturn disk were processed by separating them into latitude bins 3° wide, fitting the dependence on emission angle θ to low-order Legendre polynomial expansions, and then analyzing the thermal structure at each latitude separately. Figure 2 shows the average intensities at $\mu = \cos\theta = 0.3$. Latitudinal temperatures differed by 2.5 K. The cold equatorial zone coincides with the bright yellow band seen in visible light (3). The IRR viewing geometry (Fig. 1) limits the range of useful latitudes from 40°S to 12°N.

We may integrate the intensities $I_{20}(\mu)$ and $I_{45}(\mu)$ with respect to μ to get the fluxes and equivalent blackbody temperatures T_{20} and T_{45} for the two channels, respectively. Averaging these gives a simple estimate of the effective temperature T_e, defined so that the emitted power per area is σT_e^4. These results are given for a belt and a zone in Table 1. From Fig. 2, values at these latitudes bracket all the planet for which we have data. The effective temperature for the planet by this simple scheme is then 94.3 K. Other schemes give values between T_{20} and T_{45}.

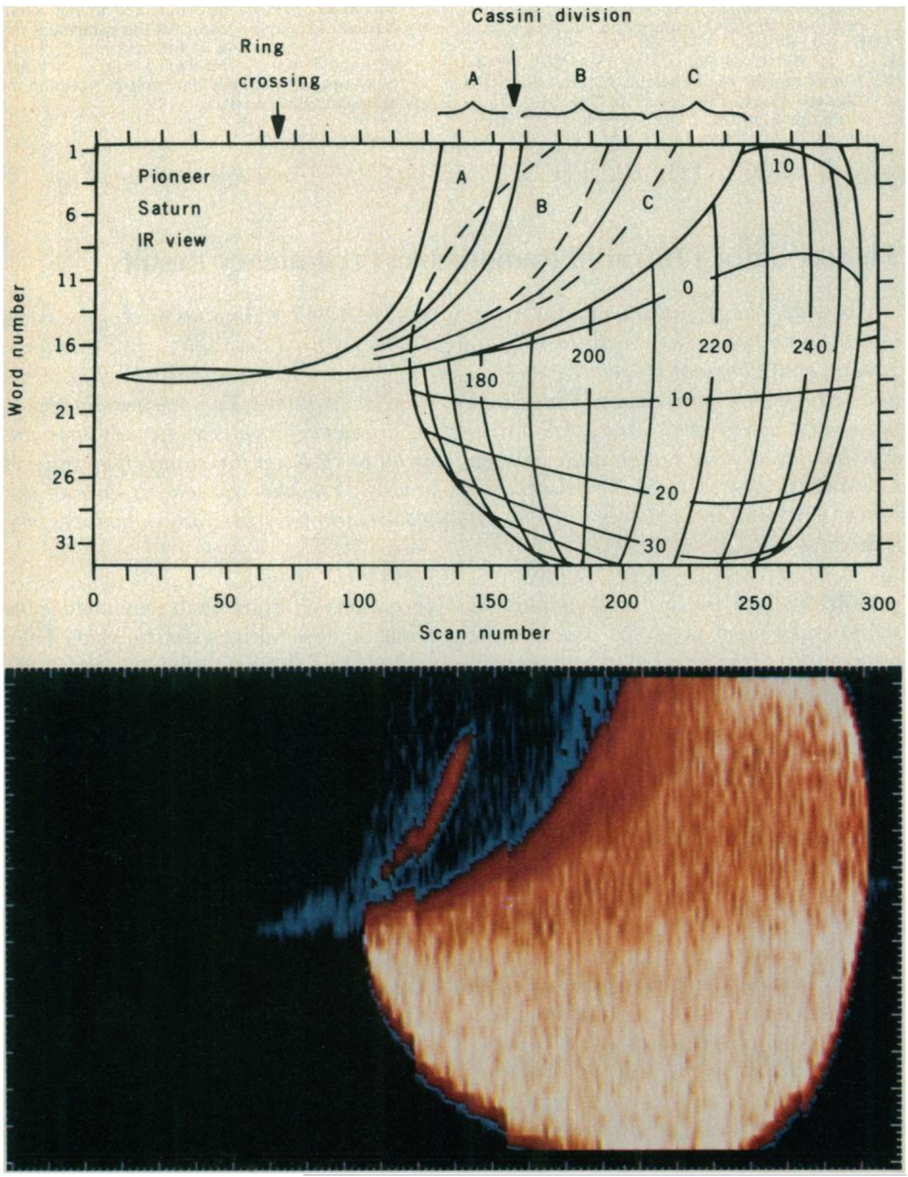

Fig. 1. Infrared image of Saturn and its rings at a wavelength of 45 μm. Scans are 30.4 seconds apart. The plane of the ring was crossed after scan 69 at 2.93 Saturn radii (R_S) from the center, and periapsis occurs following scan 300 at 1.35 R_S. The considerable image distortion is caused by the changing geometry during this 2.5-hour view period. The upper part of the figure provides a guide to features visible in the lower 45-μm image. Boundaries of the A, B, and C rings and the Cassini division are shown as solid lines curving upward. The limb of the planet behind the rings, the boundary between the inner and outer parts of the B ring, and a division within the C ring are shown as dashed lines. The north (unilluminated) side of the rings is in the field of view before scan 69. The south side in the planet's shadow is in the field of view after scan 289. Latitutdes and longitudes on Saturn are shown as solid lines, with south at the bottom. In the 45-μm image, brightness temperatures from 0 to 70 K are displayed from black to blue. Brightness temperatures from 70 to 104 K are displayed from red to white. In addition, a mean limb-darkening factor has been removed for views of the planet through the C ring and through space. This procedure increases the visibility of the cold equatorial zone from 7°S to 7°N and introduces a relatively small discontinuity at the already substantial transition between the B and C rings. Discontinuous word shifts (such as those after scans 136 and 167) occur at the spacecraft; they are taken into account in the quantitative data anslysis. The 20-μm image (not shown) exhibits the same planetary features but with a lower signal-to-noise ratio. The rings are detectable at 20 μm only by their masking of the planet.

Probably a more accurate estimate is obtained by solving for the atmospheric temperature structure that best fits the observations, assuming we know the opacity sources, and then calculating T_e. The opacity model was developed for Pioneer Jupiter data (4) and was tested by Voyager (5). The method provides a means of calculating the contribution of the 50 percent of the spectrum that was not directly observed by the IRR. The results are summarized in Table 1.

We assume that the opacity is dominated by collision-induced dipole absorption of H_2. Then channel 1 (20 μm) is sensitive to temperatures in the range from 0.1 to 0.06 bar, and channel 2 (45 μm) to temperatures in the range from 0.6 to 0.1 bar, provided we have data over $0.2 \leq \mu \leq 1.0$. This sensitivity results in essentially continuous vertical coverage from 0.6 to 0.06 bar, although it provides only minimum overlap in coverage necessary to solve for α_{H_2}, the molecular abundance of H_2 relative to H_2 + He. The overlap is less than that for Jupiter (4), largely because of the lower gravity and lower temperatures on Saturn.

Deeper than the 0.6-bar level, an adiabatic lapse rate was assumed in the model. Above the 0.06-bar level, temperature was assumed to increase with height at a rate of 35 K per decade of pressure, consistent with lapse rates in the lower stratosphere as inferred from ground-based observations (6).

For the zone at 0° to 3°S, we have data spanning the range $0.1 \leq \mu \leq 1.0$. This range provides some overlap between channels, yielding a formal estimate of $\alpha_{H_2} = 0.85 \pm 0.15$. The closeness of this estimate to the solar composition value gives us greater confidence in the opacity model and in our temperature retrieval. A more precise estimate will be obtained by comparing the derived temperature profiles of the IRR and radio occultation experiments (7).

The retrieved temperature structures are shown for $\alpha_{H_2} = 0.85$ in Fig. 3. Minimum temperatures are 83 to 85 K, and temperatures at the 1-bar reference level are 137 to 140 K. The zone is cooler than the belt at high altitudes up to the 0.06-bar level. At low altitudes, we may modify the model for the zone by adding a blackbody emitter (the cloud) at such an altitude that temperatures in the adiabatic portion equal those in the belt. This procedure places the altitude of the cloud at 119 K, between 0.6 and 0.7 bar or slightly above the level of the scattering layer inferred from polarimetric data (*3*). For Jupiter, the same method placed the cloud at 148 K (*4*). If the cloud is NH_3 on both Jupiter and Saturn, with the same condensation temperature at cloud base, the lower cloud-top temperature implies a thicker cloud for Saturn (that is, particles carried to greater heights).

The effective temperatures computed by the model are not significantly different from those calculated by the simpler method (Table 1). The ± 3 K uncertainty, as for Jupiter (*2*), covers all potential sources of error, and is largely attributable to uncertainty in the absolute calibration. The derived value $T_e = 94.4 \pm 3$ K is consistent with ground-based estimates (*8*), provided the belt and zone are representative of other latitudes. For an albedo of 0.45 ± 0.15 (*8, 9*), the ratio of total planetary emission to sunlight absorbed is 2.2 ± 0.7, and the average internal heat flux is 2.4 ± 0.8 W m^{-2}. The latter values are higher than those predicted from models of Saturn's cooling history (*10*), which suggests an additional internal energy source such as gravitational separation of He and H_2. Such separation would raise the H_2 to He ratio in the atmosphere relative to that in the interior. These statements may be revised when a new estimate of Saturn's albedo is derived.

The IRR viewing geometry (Fig. 1) offers views of the rings against space and of the rings against the planet, at instrument elevation angles with respect to the ring plane ranging from about 1° (word 18) to 30° (word 1). A threefold change in transmitted planetary radiation at the inner and outer edges of Cassini's division and at the inner edge of the B ring permits accurate determination of the radial locations of these boundaries (Table 2). The assigned uncertainties reflect our sensitivity to the spacecraft trajectory. The outer edge of the A ring appears as a transition from cold ring to colder space, and so its location cannot be determined to the same precision. The inner edge of the C ring is also a low-contrast transition. We see transmission through the B ring only at radii less than 1.65 Saturn radii (R_S) ($R_S \equiv 6 \times 10^4$ km), and have labeled this transition in Table 2. Finally, there appears to be slightly greater transmission at 1.47 R_S than on either side, which suggests a division within the C ring.

Table 2. Ring locations and normal optical depths.

Radius (6×10^4 km)	Name	τ (45 μm)
2.26 ± 0.02 2.03 ± 0.01	A Ring	0.5
2.03 ± 0.01 1.95 ± 0.01	Cassini division	0.1
1.95 ± 0.01 1.65 ± 0.02	B ring (outer)	≥1.0
1.65 ± 0.02 1.54 ± 0.01	B ring (inner)	0.5
1.54 ± 0.01 1.30 ± 0.05	C ring	0.1
1.47 ± 0.03	C ring division	0.05

Table 3. Ring temperatures at a solar elevation angle of 2.83°.

Temperature	Instrument elevation angle
South (illuminated) side	
70 K	≤ 2°
60 K	≥ 5°
South side in planet's shadow	
< 60 to 67 K	≤ 2°
North (unilluminated) side	
≈ 55 (< 60 K)	≤ 2°

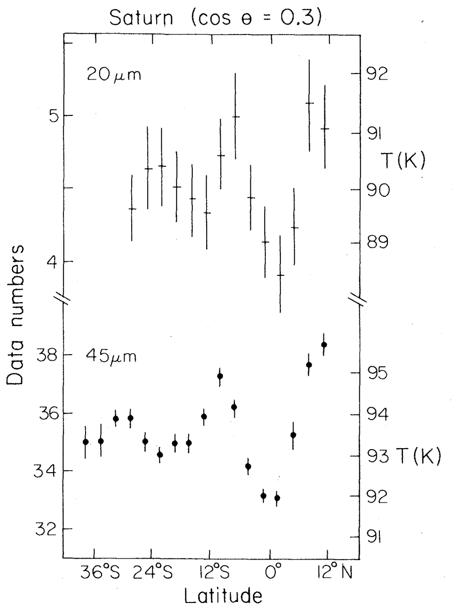

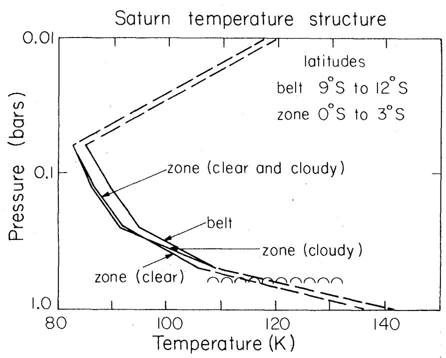

Fig. 2 (left). Latitudinal thermal structure on Saturn. The 20- and 45-μm intensities at cos $\theta = 0.3$ are plotted against latitude, with data numbers at left and a brightness temperature scale at right. Error bars, computed from the scatter of data within each 3° latitude bin, do not take into account absolute calibration uncertainties. The appearance of the cold equatorial zone (7°S to 7°N) and the warm belts to the north and south (for example, 7°S to 13°S) in both channels, suggests that the 2.5 K temperature difference extends over at least a twofold range of pressure. Features in the two channels are less well correlated south of 13°S. Fig. 3 (right). Saturn temperature structure for a belt (9°S to 12°S) and a zone (0° to 3°S). The pressure scale is logarithmic. Limb-darkening data in the 20- and 45-μm channels are inverted for temperatures in the 0.06- to 0.6-bar range. Constant lapse rates are assumed above and below, consistent with ground-based data (*6*) and an adiabatic lower atmosphere. For the belt and clear zone models, the only sources of opacity are H_2 and NH_3. For the cloudy zone model, a black emitting surface has been added at a depth chosen so that the belt and zone adiabats are the same. The cloud thus defined lies at a pressure of about 0.65 bar. Above the cloud, the 2.5 K temperature difference between belt and zone persists to great heights. For all models, a value of the ratio $\alpha_{H_2} \equiv H_2/(H_2 + He)$ of 0.85 is assumed.

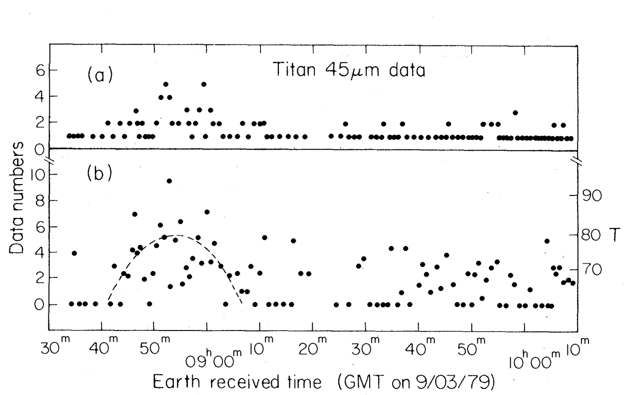

Fig. 4. Titan data at a wavelength of 45 μm. Since Titan did not fill the IRR field of view, only disk-averaged brightness is measured. Each dot corresponds to a roll of the spacecraft for which data were received. The 75.42° cone of the 45-μm field of view moved from day to night across the morning terminator of Titan during an interval centered at 8 hours (*h*) 55 minutes (*m*). Titan nominally appears once per roll, usually at word 20 (as described in the caption of Fig. 1). (a) Raw data numbers at word 20 as a function of time. (b) A sum computed from data numbers at words 18 to 22, with the expected mean curve for a brightness temperature of 80 K. The temperature scale at the right corresponds to the central value of the dashed curve.

Ring optical depths (Table 2) are determined from the transmitted intensity and are calculated for normal incidence by assuming a simple exp $[-\tau/\mu]$ law of absorption. For A and B rings and Cassini's division, emission from the rings is subtracted out by comparing the rings against the planet with the rings against space at the same elevation angles. For the C ring, for which we have no good views against space, the emitted ring intensity is small compared with the transmitted planet intensity; thus the emitted intensity can be modeled in simple ways, as by assuming a single ring temperature and assuming emissivity = 1 − transmissivity. In all the above calculations, the planetary intensity in the north behind the rings is taken to be the same as the observed intensity at the same latitude and emission angles in the south. These optical depths are essentially the same as those at optical and radio wavelengths (*11*).

As seen qualitatively in Fig. 1 (scans 100 to 150), brightness temperatures of the rings drop from 70 to 60 K as the instrument elevation angle increased from 1° (word 18) to 6° (word 15). This drop occurs whether the rings are viewed against the planet or against space, so the effect probably signifies a temperature decrease within the rings. Such a decrease is expected as a result of the low value (2.83°) of the solar elevation angle at the time of Pioneer encounter (*12*). Only a thin outside layer of optical thickness $\tau \approx \sin(2.83°)$ receives sunlight directly. Layers deeper within the ring receive less sunlight, yet they can cool to space through the thin warmer layer. When the rings are viewed at elevation angles less than ~ 2.83°, more of the thin outside layer is seen. This effect may also depend on phase angle, but the Pioneer IRR views at a fixed 75° angle with respect to incoming sunlight. The variation of ring temperatures with emission angle may complicate our derivation of the optical depth of the C ring.

Maximum ring brightness temperatures viewed with the rings against space are summarized in Table 3. Many of these views are at extremely low instrument elevation angles, so it is difficult to separate the A, B, and C rings. The coldness of the north (unilluminated) side at elevation angles ≤ 2° implies little thermal contact and little cross-plane motion during 1/4 of an orbital period. Our estimated upper limit of 60 K is approximately equal to the expected temperature of a plane sheet that is in equilibrium with planetary reflected and emitted radiation at the radius of the B ring (*12*). On the south side, the maximum observed temperature of 70 K is somewhat warm for the same plane sheet receiving sunlight at a 2.83° elevation angle in addition to planetary radiation. However, temperatures above 70 K are possible for the thin outermost layer that is in the direct solar beam and for the optically thin C ring (*13*).

South-side temperatures of the rings in the planet's shadow range from 67 to below 60 K. Although uncertainties in pointing the instrument prevent a complete separation between the A, B, and C rings, the higher temperatures seem to be associated with the C ring. Further analysis of the trajectory should significantly resolve this uncertainty. Ground-based data (*14*) show that a significant drop of about 10 K occurs when the ring particles enter the planet's shadow. Our data are not inconsistent with these observations.

It is premature to draw from these data conclusions concerning the size of particles in the rings, thermal inertia, and motion out of plane. We have found a significant temperature gradient across the rings, both from comparing the north (unilluminated) side with the south side, and from comparing the south side with itself at different instrument elevation angles. If the particles form a monolayer (*15*), these temperature differences must exist on single particles. The particles would have to be large enough (≳ 10 cm) to prevent significant heat conduction from hot to cold sides. The spin periods could not be significantly less than the orbital periods, or else the spin vectors would have to be aligned with the orbital vector. If the particles form a cloud with randomly aligned orbital inclinations (*12*), the particles will be traversing the ring plane from the thin sunlit layer on the south to the cold unilluminated layer on the north. Consequences of this changing thermal environment must be worked out and tested against observation.

Because Titan was encountered at such a great distance, it did not fill the field of view of the IRR instrument. About 30 scans were obtained over the 24-minute period when Titan was at least partly visible (Fig. 4). Quantitative analysis is complicated by several factors. First, the discontinuous word shifts visible in the Fig. 1 image tend to move the position of Titan from one word to the next and back in a sawtooth pattern. Second, the instrument's response to small objects depends on its time constant, which is not well known. Finally, the instrument has a threshold response at low intensities; that is, it cannot sense below DN = 1 even though an intensity of 0 corresponds to DN ≈ 0. These difficulties can be overcome. The upper portion of Fig. 4 shows the raw data numbers at word 20 as a function of time. With various assumptions, including the manufacturer's 10-msec estimate of response time, the disk-average brightness is 77 ± 10 K from the word 20 data. The lower portion of Fig. 4 shows a more processed quantity computed from words 18 to 22. The corresponding brightness temperature estimate of 80 ± 10 K is independent of instrument response time and is our preferred value. Such temperatures are not inconsistent with ground-based data (*16*).

A planetwide emission temperature of 80 K corresponds to an albedo of 35 percent at Titan's distance from the sun. If Titan's albedo is below this value (*9*) the discrepancy might be attributed to the fact that the IRR observed Titan on its coldest side—on the morning terminator. However, the ± 10 K uncertainty in our estimate probably renders such effects undetectable.

A. P. INGERSOLL
Division of Geological and Planetary Sciences, California Institute of Technology, Pasadena 91125
G. S. ORTON
Earth and Space Sciences Division, Jet Propulsion Laboratory, California Institute of Technology, Pasadena 91103
G. MÜNCH
Max-Planck-Institut für Astronomie, 6900 Heidelberg-Königstuhl, Federal Republic of Germany
G. NEUGEBAUER
Division of Physics, Mathematics, and Astronomy, California Institute of Technology
S. C. CHASE
Santa Barbara Research Center, Goleta, California 93017

References and Notes

1. S. C. Chase, R. D. Ruiz, G. Münch, G. Neugebauer, M. Schroeder, L. M. Trafton, *Science* **183**, 315 (1974); M. L. Bender *et al.*, *Appl. Opt.* **13**, 2623 (1974).
2. A. P. Ingersoll *et al.*, *Science* **188**, 472 (1975); A. P. Ingersoll, G. Münch, G. Neugebauer, G. S. Orton, in *Jupiter*, T. Gehrels, Ed. (Univ. of Arizona Press, Tucson, 1976), p. 197.
3. T. Gehrels *et al.*, *Science* **207**, 434 (1980).
4. G. S. Orton, *Icarus* **26**, 125 (1975); ——— and A. P. Ingersoll, in *Jupiter*, T. Gehrels, Ed. (Univ. of Arizona Press, Tucson, 1976), p. 206.
5. R. Hanel *et al.*, *Science* **204**, 972 (1979).
6. A. Tokunaga and R. D. Cess, *Icarus* **32**, 321 (1977); J. Caldwell, F. C. Gillett, I. G. Nolt, A. Tokunaga, *ibid.* **35**, 308 (1978).
7. A. J. Kliore, G. F. Lindal, I. R. Patel, D. N. Sweetnam, H. B. Hotz, T. R. McDonough, *Science* **207**, 446 (1980).
8. G. H. Rieke, *Icarus* **26**, 37 (1975); I. G. Nolt, W. M. Sinton, L. J. Caroff, E. F. Erikson, D. W. Strecker, J. V. Radostitz, *ibid.* **30**, 747 (1977); E. F. Erickson, D. Goorvitch, J. P. Simpson, D. W. Strecker, *ibid.* **35**, 61 (1978); R. Courtin, P. Léna, M. De Muizon, D. Rouan, C. Nicollier, J. Wijnbergen, *ibid.* **38**, 411 (1979); D. Gautier and R. Courtin, *ibid.* **39**, 28 (1979).
9. M. Podolak and R. E. Danielson, *ibid.* **30**, 479

(1977); M. G. Tomasko, in *Jupiter*, T. Gehrels, Ed. (Univ. of Arizona Press, Tucson, 1976), p. 486.
10. J. B. Pollack, A. S. Grossman, R. Moore, H. C. Graboske, Jr., *Icarus* **30**, 111 (1977).
11. A. F. Cook, F. A. Franklin, F. D. Palluconi, *ibid.* **18**, 319 (1973); F. P. Schloerb, D. O. Muhleman, G. L. Berge, *ibid.* **39**, 214 (1979); J. B. Pollack, *Space Sci. Rev.* **18**, 3 (1975).
12. Y. Kawata and W. M. Irvine, *Icarus* **24**, 472 (1975); I. G. Nolt, E. W. Barrett, J. Caldwell, F. C. Gillett, R. E. Murphy, J. V. Radostitz, A. T. Tokunaga, in preparation.
13. R. E. Murphy, *Astrophys. J. Lett.* **181**, L87 (1973); I. G. Nolt, A Tokunaga, F. C. Gillett, J. Caldwell, *ibid.* **219**, L63 (1978).
14. H. H. Aumann and H. H. Kieffer, *Astrophys. J.* **186**, 305 (1973); D. Morrison, *Icarus* **22**, 57 (1974); G. Neugebauer *et al.*, in preparation; G. H. Rieke *et al.*, in preparation.
15. A. Brahic, *Astron. Astrophys.* **54**, 895 (1977); P. Goldreich and S. Tremaine, *Icarus* **34**, 227 (1977).
16. D. M. Hunten, in *Planetary Satellites*, J. A. Burns, Ed. (Univ. of Arizona Press, Tucson, 1977), p. 420; J. Caldwell, *ibid.*, p. 438.
17. We thank the members of the Pioneer Project and the Deep Space Network, particularly the staff at the Madrid Tracking Station during the IRR viewing period of Titan. The able assistance of G. W. Garneau of the Image Processing Laboratory is gratefully acknowledged. Conservations with P. Goldreich, B. M. Jakosky, and D. O. Muhleman have been most helpful.

3 December 1979

Impact of Saturn Ring Particles on Pioneer 11

Abstract. *The particle flux measured by the meteoroid detectors on Pioneer 11 increased greatly while the spacecraft was near the rings of Saturn. The data suggest that the particles were associated with the rings and were not interplanetary meteoroids concentrated near the planet by gravitational focusing. The data also suggest that the E ring may be 1800 kilometers thick with an optical thickness greater than* 10^{-8}.

The meteoroid detection instrument on Pioneer 11, which was designed to determine the concentration of meteoroids with masses in excess of 10^{-8} g in the asteroid belt (*1*), detected several particles near the rings of Saturn.

The instrument has 234 detectors, consisting of pressurized cells with stainless steel walls 50 μm thick, distributed between two independent data channels. As the gas leaks from a cell after its penetration by a particle, the internal pressure passes through a limited region in which a pressure monitoring device produces a signal that causes the counter for that channel to advance and then to become inhibited for 77 minutes to allow time for all the gas to leak out of the cell (*2*). Particles that penetrate other cells on that channel while the counter is inhibited are not detected. This 77-minute dead time did not have a significant effect on the data obtained in interplanetary space because the mean time between impacts was about 27 days. However, this feature of the instrument severely limited its ability to measure the magnitude of the particle population near Saturn.

In most cases, all of the gas will escape in less than 2 seconds (*2*). There is, however, a small chance that such an extremely small hole might be produced by a penetration near threshold that the cell would still contain enough gas after the 77-minute inhibitory period to trip the counter again and start another inhibitory period.

The counters indicated that 87 cells were punctured prior to the encounter with Saturn, leaving 147 active cells as the spacecraft approached the planet.

At least four particles penetrated the detectors in the 4.5-hour period around periapsis, at least two on each data channel. The time and range of the spacecraft when the counters advanced are shown in Fig. 1. The reason for the uncertainty in the number of particles detected is that the third count on channel 0 occurred 72 to 82 minutes after the second count. If the count occurred at 77 minutes it could have been the result of a slowly leaking cell, and only four particles would then have been detected. If the count occurred between 77 minutes and 82 minutes, then five particles were detected. In either case, the counters were inhibited for approximately 70 percent of the 4.5-hour period so that other impacts probably occurred but were not detected. The penetration flux near Saturn was at least 1000 times that in interplanetary space at 9.4 AU.

The meteoroid flux measured by a penetration detector is expected to increase as a spacecraft approaches a planet because the gravitational field of the planet accelerates and focuses the interplanetary meteoroids. The data obtained near Jupiter by Pioneer 10 and Pioneer 11 are in agreement with gravitational focusing theory (*3*). The data obtained near Saturn, however, cannot be explained by gravitational focusing. It is not the total number of particles detected near Saturn, but rather the distribution with respect to radial distance that is inconsistent with gravitational focusing. All impacts occurred between 1.36 and 3.1 Saturn radii (R_S); no impacts occurred between 3.1 and 425 R_s. Gravitationally focused meteoroids should have produced twice as many penetrations between 3.1 and 50 R_s as between 1.36 and 3.1 R_s, if the mass distribution index of the meteoroids is -0.34 [as the Pioneer 10 and Pioneer 11 data suggest for the range between 10^{-8} and 10^{-9} g (*3*)]. Therefore, it is unlikely that any of the particles detected near Saturn were meteoroids. They were probably particles associated with the rings, that is, ring particles themselves or particles ejected from the rings because of collisions.

The two particles detected just before the first crossing of the ring plane could be E ring particles. These particles were detected 900 km above the ring plane (0.28°N latitude), which suggests that the E ring may be 1800 km thick. Particles could remain in inclined orbits for some time in this tenuous ring without colliding with other ring particles.

The time between these two impacts was 24 to 120 seconds. If it is assumed that this interval is representative of the mean time between the impacts of penetrating particles on the active cells in the E ring, and if it is further assumed that the size distribution of the E ring particles is meteoroidal (*4*), then the optical thickness of the E ring is calculated to be 1×10^{-8} to 5×10^{-8}. Of course, if the ring particles are not uniformly distributed throughout the 1800-km-thick ring, but are concentrated more heavily near the equatorial plane, the above optical thickness is a lower limit.

The calculated reduction in spacecraft speed due to the impact of particles during one passage through such a ring is

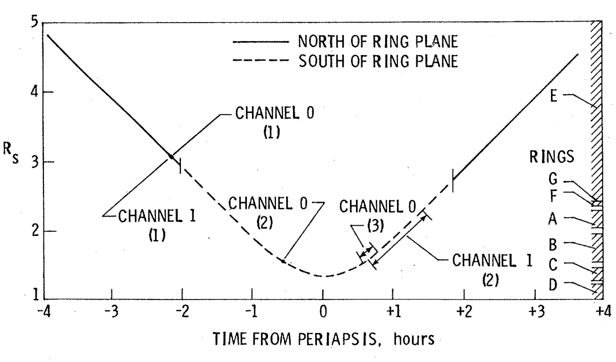

Fig. 1. The range of the Pioneer 11 spacecraft with respect to Saturn during encounter, showing the ranges and times at which particle impacts were detected by the meteoroid detection experiment.